Vacuum arc deposition of Al$_2$O$_3$–ZrO$_2$ coatings: arc behavior and coating characteristics

I. Zukerman · V. N. Zhitomirsky · G. Beit-Ya'akov ·
R. L. Boxman · A. Raveh · S. K. Kim

Abstract Al$_2$O$_3$–ZrO$_2$ coatings were deposited using a vacuum arc deposition system equipped with two co-planar cathodes. The plasma was injected into a cylindrical magnetic duct through annular anode apertures toward a substrate or an electrostatic ion current probe positioned on the duct axis, in vacuum and in a low-pressure oxygen or argon + oxygen background. Ion current and arc voltage measurements and visual observation of the cathode spots were used to find stable arcing conditions, using a straight plasma duct configuration. The cathode spot operation and transport of the plasma beam in the duct were studied as a function of arc current (I_{arc} = 25–200 A) and oxygen or oxygen + argon pressures (P = 0.1–1.5 Pa). Coatings were fabricated by exposing Si or WC–Co substrates simultaneously to Al and Zr plasmas using a 1/8 torus filter configuration in O$_2$ + Ar pressures. The coating composition, structure, microhardness, adhesion, and wear behavior were studied as functions of the deposition parameters. Favorable conditions for stable arcing were obtained with I_{arc} = 75 and 100 A for Al and Zr plasmas, respectively. The ion current decreased, and the arc voltage increased with the oxygen pressure. Behavior of the ion current and arc voltage suggested that cathode poisoning started at P = 0.5 Pa. Deposition rates were 0.3-0.6 μm/min, depending on the substrate position. All coatings were "Zr rich", i.e., the Zr:Al ratio was in the range of 1.2–5.6 depending on the substrate position and deposition conditions. The coatings with higher ZrO$_2$ concentration were harder and had better resistance to wear. The coating's hardness reached a maximum of ∼22–24 GPa at a deposition temperature of 500 °C or a negative bias voltage of 75–100 V.

Introduction

Oxides, e.g., Al$_2$O$_3$, are promising as wear-resistant coating materials for protecting cutting tool edges during high temperature operation, due to their superior high temperature stability [1]. However, being ionic compounds, they are generally more brittle than carbides and nitrides of transitional metals and also less adherent to tool substrates [2].

Al$_2$O$_3$ and ZrO$_2$ coatings, as well as Al$_2$O$_3$–ZrO$_2$ coatings with different Al$_2$O$_3$:ZrO$_2$ ratios were studied previously. Al$_2$O$_3$ is used in cutting tool applications as a bulk material for cutting inserts, and in wear-resistant coatings for cutting tools—as an intermediate or top layer in multilayer coatings [1, 3]. Al$_2$O$_3$–ZrO$_2$ coatings were deposited by various techniques, such as electrochemical deposition [4] and plasma spray [5–7] which were used for thick coatings as well as physical vapor deposition (PVD) [8–11], mainly used for thin coating deposition. Addition of ZrO$_2$ to Al$_2$O$_3$ improved mechanical properties in structural bulk ceramics [12], and thick Al$_2$O$_3$–ZrO$_2$ coatings deposited by plasma spray [6, 7] and electron beam evaporation [8]. ZrO$_2$ is presently used mainly for

I. Zukerman (✉) · V. N. Zhitomirsky · G. Beit-Ya'akov ·
R. L. Boxman
Electrical Discharge and Plasma Laboratory,
Faculty of Engineering, Tel-Aviv University,
POB 39040, Tel-Aviv 69978, Israel
e-mail: idozukerman@gmail.com

I. Zukerman · A. Raveh
Department of Chemistry, NRC-Negev, POB 9001,
Beer-Sheva 84190, Israel

S. K. Kim
School of Materials Science and Engineering,
University of Ulsan, Ulsan 680-749, South Korea

optical and thermal barrier coatings [13]. Addition of Al_2O_3 to ZrO_2 stabilized ZrO_2 in its tetragonal phase (t-ZrO_2) [9]. Moreover, ZrO_2 and Al_2O_3 have almost no mutual solubility [14], and thus may be deposited as a two-phase nano-structure with greater hardness (H) than predicted by the mixture rule [15].

Most articles discussing PVD of Al_2O_3–ZrO_2 coatings focused on using Al_2O_3 to stabilize the t-ZrO_2 phase [9, 16, 17]. For example, by controlling the Al_2O_3/ZrO_2 ratio in nano-laminate coatings, t-ZrO_2 was deposited using reactive d.c. magnetron sputtering at a low substrate temperature of $T_s = 150$ °C [9]. Klostermann et al. [10] deposited Al–Zr–O coatings with various compositions at $T_s = 500$–700 °C, using pulsed magnetron sputtering of Al and Zr metal targets in argon + oxygen background gas. Their coatings consisted of a mixture of a crystalline and amorphous (a) phases: γ-Al_2O_3 with a-ZrO_2, when the ZrO_2 content was below 8 at%., or a mixture of t-ZrO_2 with a-Al_2O_3, when the Al_2O_3 content was below 7.5 at%. Amorphous or nano-crystalline minority phase in grain boundaries was conjectured by Klostermann et al. because they did not appear in the x-ray diffraction (XRD) spectra [10]. Coatings with all other compositions were XRD amorphous. The γ-Al_2O_3 coatings had $H = 30$ GPa, while the amorphous coatings had $H = 10$–13 GPa. Klostermann et al. [10] suggested that segregation to a nc-Al_2O_3/a-ZrO_2 structure (nc—nano-crystalline) is energy activated and could be accomplished with high-energy ion flux. Trinh et al. [11, 18, 19] deposited Al_2O_3–ZrO_2 coatings using various modes of magnetron sputtering at a temperature range of $T_s = 300$–810 °C. Deposition of Al_2O_3–ZrO_2 with low ZrO_2 content resulted in amorphous coatings. However, with higher ZrO_2 content, the structure changed to a nano-structure of a-Al_2O_3/c-ZrO_2 [18] (c—cubic phase) or a-Al_2O_3/t-ZrO_2 [19], depending on the deposition method.

Both Al_2O_3 [20, 21] and ZrO_2 [22] were deposited by vacuum arc deposition (VAD). Brill et al. [20] and Rosen et al. [21] reduced the crystallization temperature of Al_2O_3 by negatively biasing the substrate, and used the bias voltage, V_b, to control the energy of ions impinging onto the substrate. By these means, the formation temperature of α-Al_2O_3 was reduced from 800 to 600 °C by increasing V_b to -300 V [20], and γ-Al_2O_3 was deposited under $V_b = -300$ V and deposition temperature T_s as low as 200 °C [21]. Recently, Kim et al. [23] deposited nano-multilayerd structures of alternating Zr–O/Al–O layers using Zr and Al cathodes in a VAD system. The Zr layers contained t-ZrO nano-crystallites. Crystallites with α-Al_2O_3 structure were observed only when the substrate was negatively biased in the 100–150 V range. However, there are no published reports of multicomponent Al_2O_3–ZrO_2 coatings fabricated by simultaneously depositing of Al and Zr plasmas in oxygen background using VAD.

This article reports on the deposition of Al_2O_3–ZrO_2 coatings using a VAD system in which two cathodes were mounted on one plane [24–26]. This system was used previously for depositing multicomponent and multilayer nitride coatings [26, 27], but not for oxides. The results are divided into two parts. The first part reports on arc behavior, i.e., ion current, arc voltage, and cathode spot motion. This information was necessary to develop the Al_2O_3–ZrO_2 deposition processes. The second part reports on deposition and characterization of the Al_2O_3–ZrO_2 coatings. The coating structure, hardness, adhesion, and tribological behavior are presented and discussed.

Experimental setup and procedure

A triple-cathode VAD system was used with two variant magnetic filter configurations: (1) a straight plasma duct, described previously [24, 25] and (2) a 1/8 torus magnetic duct for macroparticle filtering. The plasma gun (Fig. 1a) was equipped with two cathodes, Al and Zr, which were mounted in two of three holes which were equally spaced along the circumference of a 100-mm diameter circle centered on the system axis [26, 27]. In this study, both cathodes had a frustum cone shape with front and back base diameters of 49 and 54 mm, respectively, and a height of 15 mm. The straight duct (Fig. 1b) mainly was used for the arc behavior part of this study. Arc current, $I_{arc} = 25$–200 A d.c. was applied between the cathodes and the grounded anode. Each cathode had its own welding power supply and trigger mechanism. The cathode-spot-produced plasma jet entered the deposition chamber via 54-mm diameter holes in the anode, coaxial with each cathode. An axial d.c. magnetic field, $B = 12$ mT, was produced by three magnetic coils connected in the same direction, and positioned co-axially with the system axis. The axial magnetic field was intended to confine the cathode spot motion on the front cathode face [27, 28] as well as to guide the plasma flow from the cathode spots via the anode aperture to the ion current probe. The front surfaces of the cathodes were situated midway between coils 1 and 2.

For most of the coating deposition study, a 1/8 torus magnetic macroparticle filter was inserted between the plasma gun and the vacuum chamber (Fig. 1c). A d.c. magnetic field of $B = 12$ mT was applied (by five coils) to the straight and curved parts of the duct. An ion probe or substrate holder was positioned at an axial distance of 150 mm from the end flange to which the plasma gun or the 1/8 torus filter was connected, i.e., approximately midway between coils 2 and 3 in Fig. 1b, and between coils 4 and 5 in Fig. 1c.

In both configurations, before arc ignition, the vacuum chamber was pumped down to an initial residual pressure
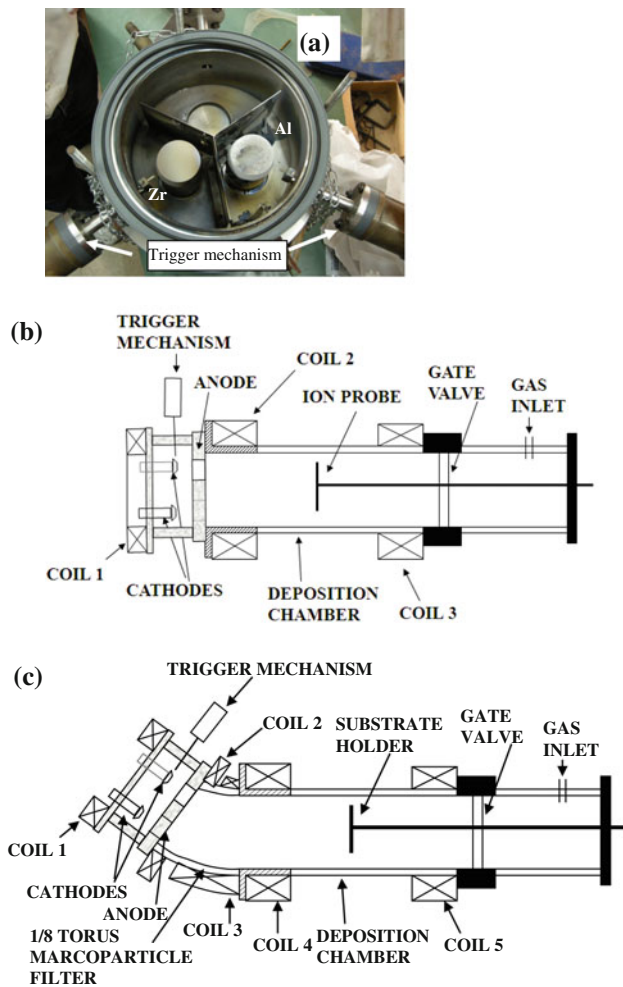
Fig. 1 Deposition systems. **a** Photograph of the plasma gun equipped with two cone-shaped cathodes, **b** schematic diagram of the vacuum arc deposition system with a straight duct, and **c** 1/8 torus macroparticle filter

lower than 0.01 Pa. The arcs were operated in vacuum (background pressure less than 0.01 Pa) and in an oxygen or oxygen + argon background pressure of $P = 0.1$–1.3 Pa. After each experiment with oxygen, the cathode was cleaned of oxides by igniting an arc in vacuum [29]. The arc parameters (arc current and voltage, ion current, etc.) were continuously recorded [29, 30].

The total ion saturation current at the probe, I_p, was measured with a 130-mm diameter flat disk probe centered on the duct axis and oriented normal to the plasma flux. A negative d.c. bias voltage, $V_b = -50$ V was applied to the probe with respect to the grounded anode to ensure I_p saturation, while minimizing the probability of igniting cathode spots on the probe [28].

Al_2O_3–ZrO_2 coatings were deposited on silicon wafer and WC–Co cutting insert substrates. The cutting insert surfaces were polished to a mirror-like finish, and the substrates were

cleaned with alcohol before deposition. Prior to deposition, the substrate was heated to the desired substrate temperature, T_s, with a 1-kW halogen lamp placed within the substrate holder [31]. T_s was measured using a thermocouple situated beneath the coated sample and regulated using a feedback control system [31]. During deposition, T_s sometimes increased due to the surface bombardment by energetic ion flux; however, this increase was not more than 20°. The coatings were deposited while simultaneously operating the Al and Zr cathodes with $I_{arc} = 75$ and 100 A, respectively, in an Ar + O_2 mixture with total pressure $P_{Ar/O_2} = 1.06$ Pa ($P_{Ar} = 0.26$ Pa, $P_{O_2} = 0.80$ Pa). In this research study, T_s, was varied between 50 and 500 °C and V_b between −50 and −200 V. The deposition time was 360 s. After deposition, the coating thickness, t, was measured using an Alpha-step profilometer. The coating's electrical resistivity, ρ, was measured by applying a silver paste on a controlled area of the coatings surface. ρ was then measured by ohmmeter between the silver paste and the Si substrate. The substrate ρ was neglected.

The coating's cross-sectional morphology was studied using scanning electron microscopy (SEM). The coating's composition was analyzed using SEM combined with energy dispersive x-ray spectroscopy (EDX). X-ray photo-electron spectroscopy (XPS) using a 5600 Multi-Technique System (PHI, USA) was applied to study the elemental distribution and oxidation status of elements in the coatings. The sample surfaces were analyzed, and then the interior after 6-min sputtering with a 4 kV Ar^+ gun (5×5 raster and 23.5 A/min sputter rate on SiO_2/Si reference samples). The crystalline structure was studied using XRD with CuK_α radiation (wavelength $\lambda = 0.1541$ nm) using a Scintag θ:θ powder diffractometer, equipped with a liquid nitrogen cooled Ge solid-state detector. The scanning range was between $2\theta = 20$ and 70°.

The coating's hardness was measured using a microhardness tester equipped with a Knoop indenter at a load of 0.1 N. Every microhardness (H_K) value was the average of five measurements. The coating adhesion was assessed by a scratch test (CSM-REVETEST) using a diamond indenter whose radius of curvature was 0.2 mm. Each scratch was 5 mm long at constant load, after which the scratch track was examined by optical microscopy. The scratch load was increased until the first appearance of coatings failure (defined as substrate exposure), determining a critical load, L_c. The tribological behavior was studied using a tribometer (CSM) against a 3″ WC ball in ambient air. The linear sliding speed was 0.1 m/s. Two sets of tests were conducted: (1) with a load of 1 N and a sliding distance of 300 m, and (2) a load of 5 N and a sliding distance of 100 m. After the wear test, the cross section of the wear track was measured using a profilometer and was used to calculate the wear coefficient, $W = V/Ls$ where V is the

removed volume, L is the load, and s is the sliding distance [32].

Results

Arc behavior and ion current measurements

Influence of the arc current on cathode spot motion and ion current

The saturated ion current, I_p, was measured as a function of I_{arc} using the straight duct configuration (Fig. 1b). For Zr arcs, increasing I_{arc} from 50 to 100 A increased I_p from 1.4 to 2.5 A. However, with further increases of I_{arc}, I_p decreased sharply, to 0.3 A at $I_{arc} = 175$ A. Visual observation of the cathode spot motion showed that initially increasing I_{arc} increased the number of cathode spots on the cathode front face. However, when $I_{arc} \geq 100$ A, the number of spots on the face decreased as they concentrated on the peripheral conical surface. At $I_{arc} \geq 150$ A, no spots were observed on the cathode front face. The same qualitative behavior was found for the Al cathode. The highest $I_p = 1.9$ A, and the most intense spot activity on Al cathode front surface were observed at $I_{arc} = 75$ A.

Influence of oxygen pressure on the arc behavior

Figure 2 shows the influence of P on I_p collected from Zr and Al cathodes, in the straight duct configuration. The open symbols represent an oxygen environment (P_{O_2}) and the solid symbols, a mixed Ar + O_2 environment (P_{Ar/O_2}). In vacuum, Al and Zr had an I_p of 1.9 and 2.5 A, respectively. Introduction of O_2 sharply decreased $(I_p)^{Al}$ to 0.9 A at $P_{O_2} = 0.2$ Pa, and then it was maintained almost constant up to $P_{O_2} = 0.5$ Pa. Further increase in P_{O_2} rapidly decreased $(I_p)^{Al}$ to 0.1 A at $P_{O_2} = 1$ Pa. For Zr, a similar trend was found, although $(I_p)^{Zr}$ decreased constantly, with a lower decrease rate in the pressure range $0.2 < P_{O_2} < 0.5$ Pa. The experiments in oxygen environment were characterized by unstable arc operation and a tendency for the arc to spontaneously extinguish.

Addition of Ar to the environment increased I_p considerably, e.g., $(I_p)^{Zr} = 3.15$ A in pure Ar at $P_{Ar} = 0.26$ Pa compared to $(I_p)^{Zr} = 2.5$ A at $P = 0.01$ Pa (vacuum). The addition of $P_{Ar} = 0.26$ Pa improved the process stability, especially for the Al cathode, as the number and amplitude of the arc voltage fluctuations decreased. It resulted in an increase of $(I_p)^{Al}$ at all P_{Ar/O_2} and an increase of $(I_p)^{Zr}$ at $P_{Ar/O_2} < 0.8$ Pa.

Investigation of the I_p and arc voltage (V_{arc}) dependence on time for various P_{O_2} showed different behavior for $P_{O_2} < 0.5$ Pa and $P_{O_2} > 0.5$ Pa. For $P_{O_2} < 0.5$ Pa,
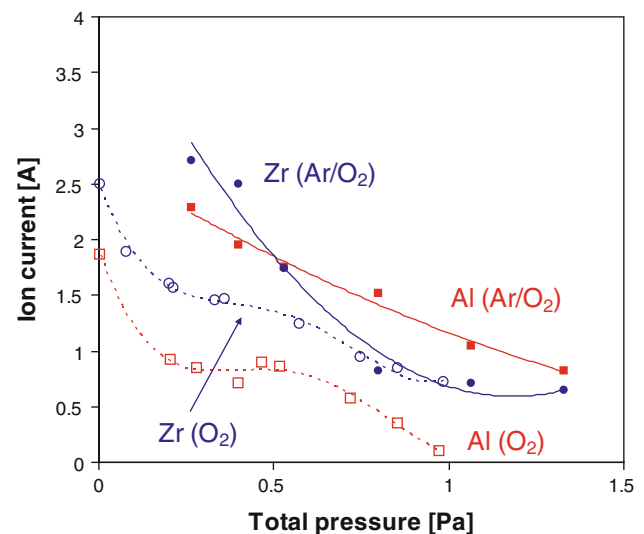

Fig. 2 Ion current as a function of total pressure with $(I_{arc})^{Al} = 75$ A, $(I_{arc})^{Zr} = 100$ A. *Open symbols* O_2 environment, *full symbols* Ar/O_2 ($P_{Ar} = 0.26$ Pa) environment

I_p decreased with time, while V_{arc} was constant. For $P_{O_2} > 0.5$ Pa, I_p decreased with time, while V_{arc} increased. This behavior was similar for both Al and Zr cathodes (although more pronounced for Al) and indicated that oxidation of the cathodes started at $P_{O_2} = 0.5$ Pa.

Deposition and characterization of Al_2O_3–ZrO_2 coatings

Based on the results described above, the deposition conditions were set to $(I_{arc})^{Al} = 75$ A, $(I_{arc})^{Zr} = 100$ A, and $P_{Ar/O_2} = 1.06$ Pa ($P_{Ar} = 0.26$ Pa, $P_{O_2} = 0.80$ Pa). Deposition of Al_2O_3–ZrO_2 coatings using the straight duct (Fig. 1b), resulted in a deposition rate of 0.5–1.0 μm/min; however, with a large number of macroparticles, a few were as big as 50 μm (Fig. 3a). In order to screen out the macroparticles, the 1/8 torus magnetic filter was added between the arc plasma gun and the straight duct (Fig. 1c).
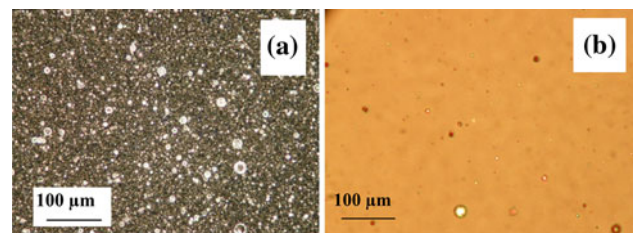
Fig. 3 Optical micrographs of the coating surfaces deposited using a straight duct system (**a**) and the 1/8 torus magnetic filter (**b**). Both coatings were deposited at $V_b = -50$ V and without substrate heating. The substrates were located 150 mm from the anode, and the deposition time was 360 s

The filter reduced the macro-particle number considerably (Fig. 3b), while reducing the deposition rate by only 50%.

In both configurations (with and without the 1/8 torus filtered), two regions were identified on the substrate holder: (1) the projection of Zr ion beam which was called the Zr region, and (2) the projection of the Al ion beam which was called the Al region. Si samples were positioned at the centers of the two regions. Table 1 presents the thicknesses and compositions of the coatings from these two regions deposited using the filtered configuration (Fig. 1c). The concentration presented as ZrO_2 and Al_2O_3 content was calculated from the atomic concentration determined by EDX and XPS. It should be noted that calculation of Zr:Al:O atomic ratio obtained from EDX studies indicated that the coatings consist of a mixture of approximately stoichiometric ZrO_2 and Al_2O_3, i.e., no excess or deficiency of O was found. The coatings of both regions were zirconia rich. The Zr region coating thickness was 3–4 μm (deposition rate of ~ 0.6 μm/min) and the Al region coating thickness was 1.5–2.0 μm (deposition rate of ~ 0.3 μm/min). The coatings in both regions were electrically insulating and transparent—multiple interference fringes were visible where the coating thickness was not uniform. ρ of a typical coating (deposited at $T_s =$ 250 °C, $V_b = -50$ V) was found to be $\rho = 4 \times 10^7$ Ω m.

Figure 4 presents high-resolution XPS spectra of the Zr3d (a, c) and Al2p (b, d) regions, before (a, b) and after (c, d) 6 min of sputtering by Ar$^+$, for coatings from the Zr and Al regions deposited at $T_s = 250$ °C and $V_b = -50$ V. The results were compared to reference samples of bulk ZrO_2 and Al_2O_3 [33]. The spectra before sputtering (Fig. 4a, b) included peaks of fully oxidized Zr and Al, i.e., a ZrO_2, doublet (Fig. 4a) and Al_2O_3 lines (Fig. 4b) were similar to the XPS spectra of reference bulk ZrO_2 and Al_2O_3 [33]. Free metal peaks were not observed. However, after sputtering, the XPS spectra were different from those at the surface; specifically some free metal was observed. The Zr3d spectrum (Fig. 4c), together with a doublet peak related to ZrO_2, had a shoulder on the lower binding energy side of the Zr–O oxide, and lower intensity peak at a binding energy of ~ 178 eV. This indicates the presence of free Zr [33, 34]. Similarly, in the Al2p spectrum (Fig. 4d) along with the oxidized Al peak, a peak at 71.5 eV appeared. This may be attributed to free Al [33, 34].

Table 1 Composition of ZrO_2 and Al_2O_3 calculated from EDX and XPS, and thickness of the coatings from Zr and Al region after deposition

	ZrO_2 content (% mol.)	Al_2O_3 content (%mol.)	Thickness (μm)
Zr region	70–88	12–30	3–4
Al region	50–75	25–50	1.5–2

However, the presence or the absence of free metal atoms within the coatings cannot be concluded from the appearance of free metal peaks in the XPS spectra after sputtering, as these peaks might be attributed to preferential sputtering of oxygen, which was described previously for ZrO_2 [34] and recently presumed for Al_2O_3 coatings [33]. XPS analysis of other coatings deposited with higher V_b (up to -200 V) did not reveal any chemical composition dependence on V_b.

The concentrations of ZrO_2 and Al_2O_3 were determined from the XPS spectra before sputtering. Taking into account that along with the above oxides, fully oxidized carbon is also present on the surface, the oxygen bound with carbon was excluded from calculation, assuming full C oxidation and CO_2 formation on the surface. Similar to EDX, XPS indicated that in both the Zr and the Al regions, the concentration of Zr was larger than that of Al. Calculations based on the XPS data showed that the Zr region coatings contained 70–88% ZrO_2 while the Al region coatings contained 50–75% ZrO_2 (Table 1).

Figure 5 shows the XRD spectrum of Zr region coatings at different T_s (Fig. 5a) and V_b (Fig. 5b). In general, the XRD spectra of ZrO_2 and Al_2O_3 are difficult to interpret, due to their large number of crystalline phases. Moreover, the sharp peaks at $2\theta = 29.5°$, 33.0°, 61.7°, and 65.8°, that could be related to m-ZrO_2 (m-monoclinic) or γ-Al_2O_3, originated from the Si substrate. Thus, the spectra in Fig. 5a ($V_b = -50$ V) indicate that the coatings were XRD amorphous, and the increase of T_s to 500 °C did not form crystalline oxides. However, with the increase in V_b ($T_s = 250$ °C), a wide peak appeared at $2\theta = 48°$, which is, most likely, due to the formation of the m-ZrO_2 crystalline phase (Fig. 5b). Coatings deposited in the Al region had XRD patterns similar to the ones in Fig. 5a for all T_s and V_b tested, and most likely, had an XRD-amorphous structure.

Figure 6 shows the Knoop hardness (H_K) of Al_2O_3–ZrO_2 coatings deposited on Si substrates as a function of T_s (Fig. 6a) and V_b (Fig. 6b). At $T_s = 50$ °C, H_K in both the Al and Zr regions of the coatings was close to H_K of the Si substrate. The H_K of the Zr region coatings increased with T_s and reached $H_K = 22$ GPa at $T_s = 500$ °C. The hardness of the Al region coatings increased only slightly with T_s. With increasing V_b, the hardness of the Zr region coatings increased to a maximum of $H_K = 22$–24 GPa at $V_b = -75$ to -100 V, and then strongly decreased to 16 GPa at $V_b = -150$ V. The Al region coatings showed the same trend as the Zr region coatings; however, with only a small maximum, $H_K = 14$ GPa at $V_b = -100$ V, compared to $H_K = 12$ GPa at $V_b = -50$ V.

Table 2 presents the critical load L_c and wear behavior of coatings deposited on WC–Co substrates. The coating's thickness was similar to those measured on Si wafers,

Fig. 4 XPS spectra before sputtering (**a**, **b**) and after 6-min sputtering by Ar + ions (**c**, **d**), Zr3*d* (**a**, **c**) and Al2*p* (**b**, **d**) local spectra. Coating deposited at $T_s = 250\ ^\circ C$ and $V_b = -50\ V$
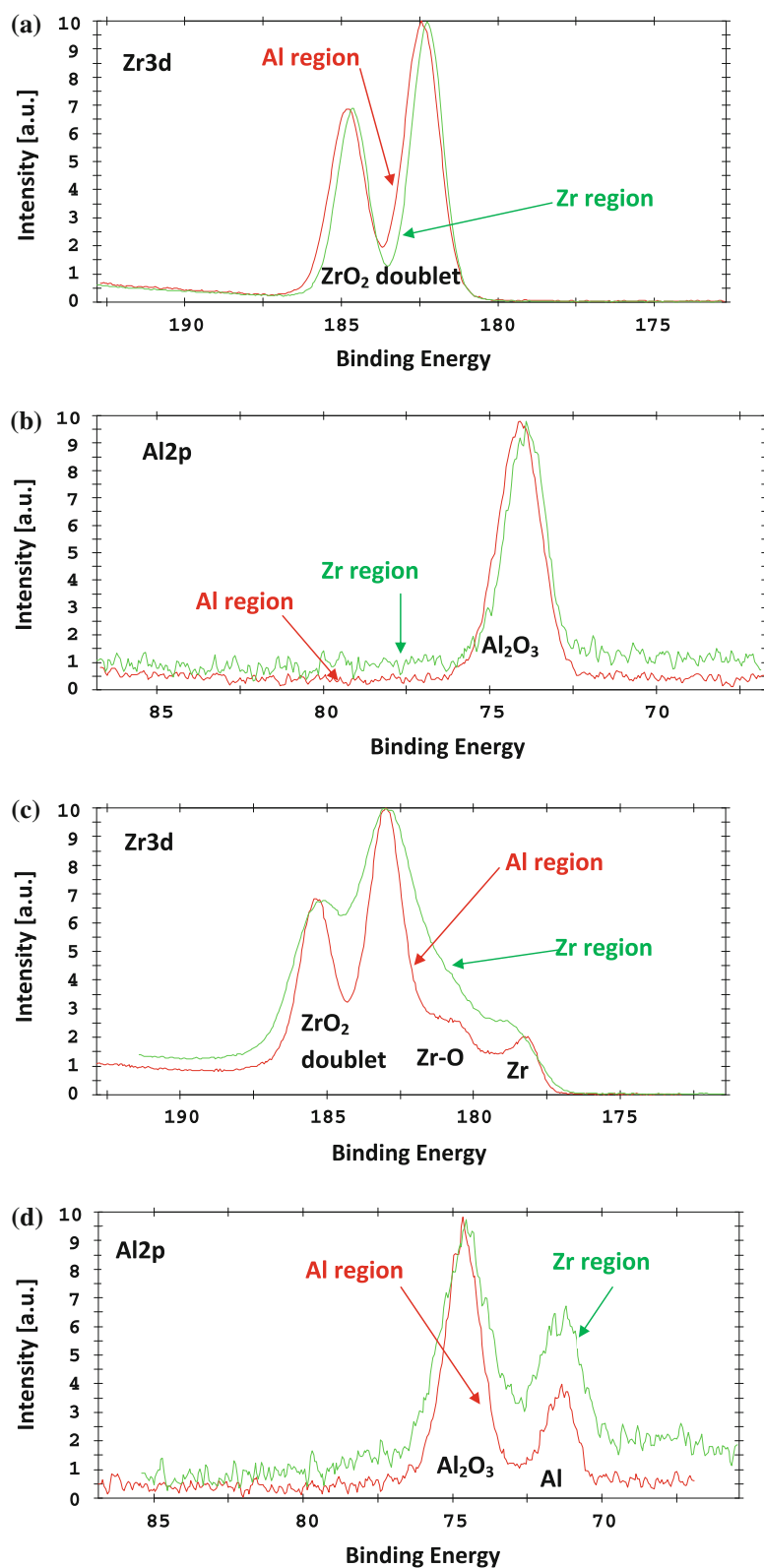
i.e., $t = 3–4\ \mu m$ at the Zr region and $t = 1.5–2.0\ \mu m$ at the Al region. Zr region, coatings deposited with $T_s = 250\ ^\circ C$ and $V_b = -50\ V$ had low $L_c = 15\ N$ and endured sliding 300 m under a load of 1 N, but failed at 5 N after a few

meters. Increasing T_s to 500 °C improved the coating properties considerably. Zr region coatings did not show adhesive failure at 100 N, which was the highest load tested, and endured 300 m at a load of 1 N and 100 m with
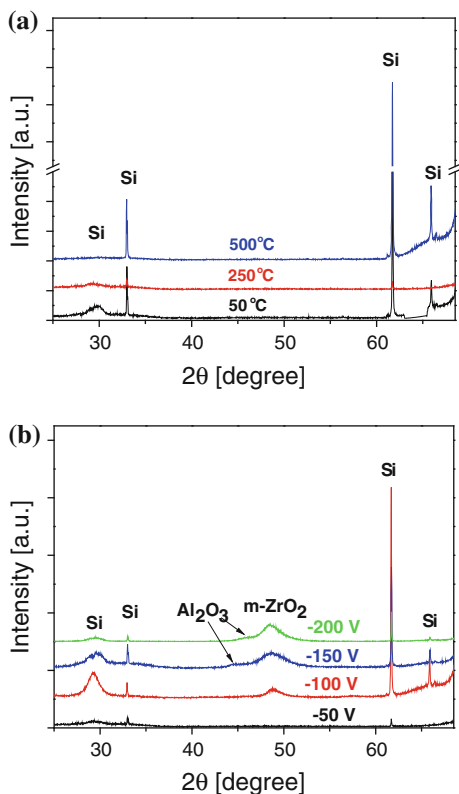
Fig. 5 XRD spectrum of Zr region coatings at: **a** various deposition temperatures ($V_b = -50$ V) and **b** various negative substrate bias ($T_s = 250$ °C)

5 N, being the longest distances tested. Increasing V_b to -100 V had only a minor effect on the coating properties. L_c of the Zr region coatings increased to 30 N, and the coating started to show wear failure at a sliding distance of 300 m (load of 1 N).

Al region coatings showed similar results (Table 2). Al region coatings deposited with $T_s = 250$ °C and $V_b = -50$ V had low $L_c = 5$ N and failed after a wear distance of 30 m (under load of 1 N). The increase of T_s to 500 °C improved L_c to more than 100 N, and the sliding distance
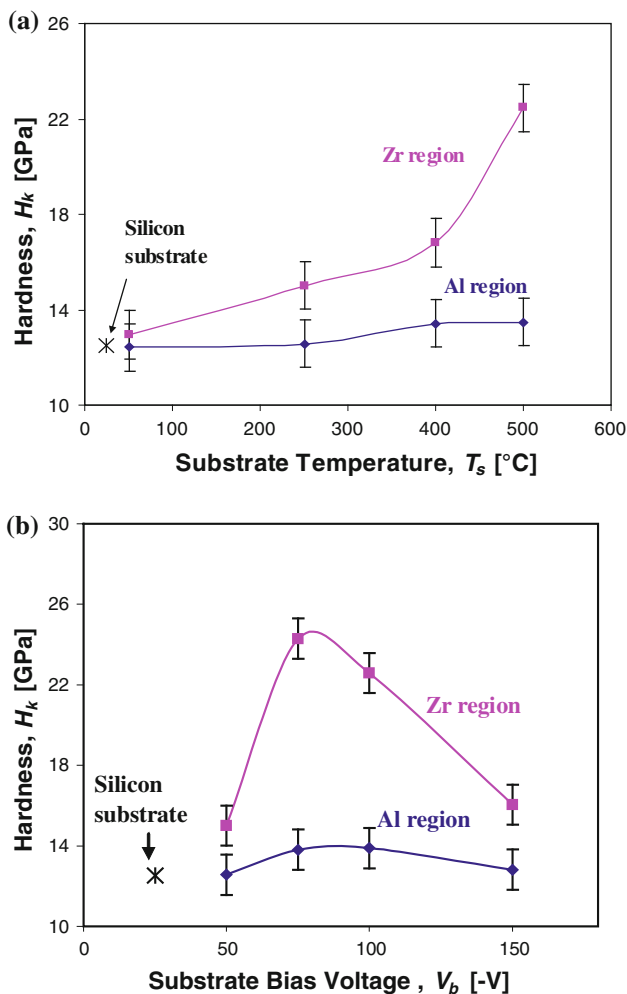
Fig. 6 Knoop hardness, H_K, of Zr and Al regions coatings as a function of: **a** substrate temperature ($V_b = -50$ V) and **b** negative bias voltage ($T_s = 250$ °C)

increased to 100 m (load of 1 N). Increasing V_b to -100 V did not change L_c (compared to coatings deposited with $T_s = 250$ °C and $V_b = -50$ V), while the sliding distance increased to 70 m (load of 1 N).

Table 2 The hardness, adhesion critical load, and wear behavior of Al$_2$O$_3$–ZrO$_2$ coating deposited on WC–Co substrates

Only coatings which endured a full-length (300 m) wear test at 1 N were tested under 5 N

	Substrate temperature, T_s (°C)	Substrate bias voltage, V_b (−V)	Scratch adhesion, L_c (N)	Distance to failure (m) [normal load (N)]	Wear coefficient (mm^3/N m)
Zr region	250	50	15	>300 (1)	1.9×10^{-6}
				<5 (5)	
	500	50	>100	>300 (1)	2.8×10^{-7}
				>100 (5)	
	250	100	30	∼300 (1)	5.7×10^{-7}
Al region	250	50	5	30 (1)	–
	500	50	>100	100 (1)	9.6×10^{-6}
	250	100	5	70 (1)	–

The wear rate W of the coatings was calculated based on the full-length (300 m, 1 N) wear tests. Table 2 shows W of the coatings which endured the full-length test. For Zr region coatings deposited with $V_b = -50$ V and $T_s = 250$ °C, W was 1.9×10^{-6} mm^3/N m. W decreased by a factor of 2 when the bias was increased to $V_b = -100$ V, and by one order of magnitude when the temperature was increased to $T_s = 500$ °C.

Discussion

In general, the cathode spot motion on the frustum cone cathode and the dependence of I_p at I_{arc} were similar to those described previously [29, 35] even though the previous cathodes were centered on the duct axis, and thus were in an axial-symmetric magnetic field, whereas the cathodes were located off-axis. As noted in the previous studies [29, 35], the number of cathode spots increased with I_{arc}, and they tended to move on the peripheral area of the cathode, and I_p tended to decrease with I_{arc} at constant B.

Oxygen affected the arc in two ways: decreasing I_p and increasing V_{arc}. These phenomena can be explained by two mechanisms: (1) cathode and anode "poisoning" (i.e., formation of an insulating oxide layer) [29], which prevented spot motion, resulting in unstable arc operation, increased V_{arc} and its fluctuation, and decreased cathode spot produced plasma flux and thus, decreased I_p [36], and (2) ion scattering from the gas molecules which lowered I_p [37]. At $P_{O_2} < 0.5$ Pa, I_p decreased with P_{O_2} while V_{arc} was constant, suggesting that only ion scattering was significant. An oxide layer on the cathode and anode probably formed only at $P \geq 0.5$ Pa, where V_{arc} increased and I_p decreased. Addition of argon stabilized the arc as was described previously [38]. In this study, introducing $P_{Ar} = 0.26$ Pa of Ar to the oxygen environment increased $(I_p)^{Al}$ by 2–3 times compared to $(I_p)^{Al}$ in O$_2$, and increased $(I_p)^{Zr}$ by 50% compared to $(I_p)^{Zr}$ in $P_{O_2} < 0.5$ Pa. These results might be due to inhibiting of the cathode surface poisoning associated with Ar addition, and thus more stable arc operation and higher cathode erosion rate.

Deposition using the straight plasma-duct-produced coatings heavily contaminated with macroparticles. Most of the macroparticles originated from the Al cathode. Bolt et al. [39] also reported almost 100% macro-particle coverage when depositing Al$_2$O$_3$ coatings with a direct line of sight between the cathode and the substrate. Using a 1/4 torus filter, they reduced the macroparticles coverage to 1% [39]. In this study, most of the macroparticles (Fig. 3) were screened using a 1/8 torus filter, while maintaining a deposition rate of 0.3–0.6 μm/min. This deposition rate in

this study was about 2–5 higher than reported previously during filtered VAD of Al$_2$O$_3$ [21, 39] or ZrO$_2$ [22].

Among the many parameters influencing VAD, V_b is one of the most important ones controlling the coating structure and properties. This was also shown paradoxically for dielectric substrate [40, 41] and in Figs. 5b and 6b of present article. In order to estimate the potential on coating surface taking into account the bias and the resistance of the coating, $\rho = 4 \times 10^7$ Ω m of a typical coating ($T_s = 250$ °C, $V_b = -50$ V) will be used. The typical ion current during deposition was 1.5 A (Fig. 2 P_{Ar/O_2} curves), and it fell on an area of $\sim 4 \times 10^{-3}$ m^2. Thus, the ion current flux, J_P, reaching the coatings surface was $J_P = 375$ A/m^2. Neglecting any voltage drop in the substrate and using equation $V = J_p\rho t$ (where t is coating thickness), the voltage drop across a $t = 3$ μm thick coating is 45×10^3 V, which makes the influence of V_b questionable. The coating thickness across which the voltage drop is equal to V_b is between ~ 3 nm (for $V_b = -50$ V) to ~ 13 nm (for $V_b = -200$ V). This implies that d.c. biasing should only be effective for a short period of time at the beginning of the deposition process, i.e., before the film reaches a thickness of 3–13 nm. One possibility is that the influence of bias on the coating structure at this early stage influences the subsequent film growth. This initial layer provides the nucleation sites of the coating and thus may strongly influence the subsequent coating structure [42]. A further possibility is that the bias voltage exceeds the dielectric strength of the thin film, and thus the film is conductive for the bias voltages applied. Another possibility is that the environment on the coating surface during deposition is far from that during post-deposition resistivity measurements at room temperature. The coating's surface is excited during deposition by particle and photon bombardment, as well as by elevated substrate temperature, which might strongly reduce the coating resistivity. Even if the bulk coating resistivity during deposition is close to the values measured after deposition, possibly surface conduction could provide a conductive path to the peripheral area of the substrate where little or no coating is deposited, and hence where the surface potential is V_b.

Two regions, each a projection of an ion beam emitted from a cathode, were identified on the substrate holder. Although the plasma beam may be steered in the present VAD system [26] (and uniform composition can be achieved by sweeping the ion beams in an X–Y pattern), in this study, we chose to study the coating composition by placing substrates at the centers of both regions. Both the Al and Zr regions coatings were ZrO$_2$ rich (Table 2).

The shape of Zr3d and Al2p peaks in XPS spectra before sputtering and the fact that the coatings have high resistance indicated that the coatings consist of only a mixture

of the fully oxidized Zr and Al, i.e., ZrO_2 and Al_2O_3. In contrast, in recently studied nano-multilayered coatings [33], a large amount of free Zr and Al metals was found. It is apparent in this study that the oxygen pressure was sufficient for oxide formation, and the filtering using the 1/8 torus magnetic filter was effective enough to remove macroparticles from the plasma flux and thus from the coatings. The XPS results before sputtering (Fig. 4a, b), which are in agreement with the EDX studies of coating concentration, indicate on approximately stoichiometric coatings. However, the exact quantification of stoichiometry is not possible due to carbon contamination on the surface as well as the preferential sputtering of oxygen in XPS analysis.

The XRD indicated that oxide crystallites formed when sufficiently high bias was applied during deposition (Fig. 5). The crystallization is possibly associated with the increased energy delivered by the impinging ions to the coating surface. Increased adatom energy, whether due to ion bombardment or higher substrate temperature, is thought to be the key in obtaining crystalline oxides [10, 20, 21]. It should be noted that in this study, coatings in the Zr region had an Al_2O_3 content which was never less than 12 mol%., i.e., larger than the maximum crystallization concentration found by Klostermann et al. [10]. Thus, it is likely that decreasing the Al_2O_3 concentration and increasing T_s could facilitate ZrO_2 crystallization in the coatings produced in our system.

Both increasing T_s and V_b increased H_K in the Zr region coatings (Fig. 6). This increase might originate from structural re-organization during deposition. Although the XRD did not indicate crystallization with increasing T_s, the increase in H_K (Fig. 6a) might be the result of the formation of crystallites sufficiently small so that they are not detected by XRD (i.e., XRD-amorphous films are produced) [43]. The Al region coatings showed only minor H_K increase, possibly due to their lower thickness, but probably due to the higher Al_2O_3 concentration. Previous studies [10, 16] found crystallization of ZrO_2 in coating with low Al_2O_3 concentration, lower than that found in the Zr region in this study, while coatings with higher Al_2O_3 concentration were amorphous. Klostermann et al. [10] low Al_2O_3 concentration coatings were harder.

The initial L_c and W results of coatings on WC substrates (Table 2) emphasize the importance of T_s and V_b during deposition on the coating tribological properties. The stronger influence of T_s on L_c and W compared to V_b might be attributed to higher intrinsic stress with high V_b. Although one cannot compare between L_c and W of the Zr and Al regions coatings due to their different thickness, the coatings composition has also a strong influence on the crystallization and hardness of the coatings [10].

The results show the important influence of T_s, V_b, and Al_2O_3 concentration on the coating properties and the potential of the Al_2O_3-ZrO_2 coating family. Given this influence, further investigations with higher T_s, lower Al_2O_3, and further combinations of T_s and V_b are recommended.

Conclusions

1. Favorable condition for deposition of Al_2O_3 and ZrO_2 coatings were arc currents of 75 and 100 A, respectively and in an Ar + O_2 mixture with total pressure $P_{Ar/O_2} = 1.06$ Pa ($P_{Ar} = 0.26$ Pa, $P_{O_2} = 0.80$ Pa).
2. The 1/8 torus magnetic filter can remove most of the macroparticles while maintaining relatively high deposition rate of 0.3–0.6 μm/min.
3. Zr region coatings deposited with appropriate values of T_s and V_b included crystallite oxides.
4. T_s (and to some extent V_b) strongly influenced the coating adhesion and wear resistance.

References

1. Klocke F, Gerschwiler K, Fritsch R, Lung D (2006) Surf Coat Technol 201:4389
2. Holleck H (1986) J Vac Sci Technol A4:2661
3. Knotek O, Löffler F, Krämer G (2001) In: Bunshah R (ed) Handbook of hard coatings deposition technologies, properties and applications. Noyes Publications, New Jersy, p 370
4. Chaim R, Zhitomirsky I, Gal-Or L, Bestgen H (1997) J Mater Sci 32:389. doi:10.1023/A:1018505517104
5. Kim HJ, Kim YJ (1999) J Mater Sci 34:29. doi:10.1023/A:1004492919174
6. Shanmugavelayutham G, Yano S, Kobayashi A (2006) Vacuum 80:1336
7. Sharafat S, Kobayashi A, Ogden V, Ghoniem MN (2000) Vacuum 59:185
8. Leushake U, Krell T, Schulz U, Peters M, Kaysser WA, Rabin BH (1997) Surf Coat Technol 94–95:131
9. Teixeira V, Monteiro A, Duarte J, Portinha A (2002) Vacuum 67:477
10. Klostermann H, Böcher B, Fietzke F, Modes T, Zywitzki O (2005) Surf Coat Technol 200:760
11. Trinh DH, Högberg H, Andersson JM, Collin M, Reineck I, Helmersson U, Hultman L (2006) J Vac Sci Technol A24:309
12. Matthews L, Rawlings RD (1994) Composite materials: engineering and science. Chapman and Hall, Oxford, p 137
13. Tay BK, Zhao ZW, Chua DHC (2006) Mater Sci Eng R52:1
14. Jerebtsov DA, Mikhailov GG, Sverdina SV (2000) Ceram Int 26:821

15. Raveh A, Zukerman I, Shneck R, Avni R, Fried I (2007) Surf Coat Technol 201:6136
16. Qadri SB, Gilmore CM, Quinn C, Skelton EF, Gosset CR (1989) Phys Rev B39:6234
17. Aita CR, Scanlan CM, Gajdardziska-Josifovska M (1994) JOM 46:40
18. Trinh DH, Ottosson M, Collin M, Reineck I, Hultman L, Hogberg H (2008) Thin Solid Films 516:4977
19. Trinh DH, Kubart T, Nyberg T, Ottosson M, Hultman L, Hogberg H (2008) Thin Solid Films 516:8352
20. Brill R, Koch F, Mazurelle J, Levchuk D, Balden M, Yamada-Takamura Y, Maier H, Bolt H (2003) Surf Coat Technol 174–175:606
21. Rosen J, Mraz S, Kreissig U, Music D, Schneider JM (2005) Plasma Chem Plasma Proc 25:303
22. Yu GO, Tay BK, Zhao ZW (2005) Appl Phys A81:405
23. Kim SK, Le VV, Boxman RL, Zhitomirsky VN, Lee JY (2010) Surf Coat Technol 204:1697
24. Ben-Ami R, Zhitomirsky VN, Boxman RL, Goldsmith S (1999) Plasma Sour Sci Technol 8:355
25. Zhitomirsky VN, Grimberg I, Boxman RL, Weiss BZ, Travitzky NA, Goldsmith S (1997) Surf Coat Technol 94–95:207
26. Zhitomirsky VN, Grimberg I, Rapoport L, Travitzky NA, Boxman RL, Goldsmith S, Weiss BZ (1999) Surf Coat Technol 120–121:219
27. Zhitomirsky VN (2007) Surf Coat Technol 201:6122
28. Boxman RL, Zhitomirsky VN (2006) Rev Sci Instrum 77:021101
29. Zhitomirsky VN, Raveh A, Boxman RL, Goldsmith S (2009) IEEE Trans Plasma Sci 37:1517
30. Zhitomirsky VN, Boxman RL, Goldsmith S (2004) Surf Coat Technol 188–189:220
31. Zhitomirsky VN, Grimberg I, Rapoport L, Boxman RL, Travitzky NA, Goldsmith S, Weiss BZ (2000) Surf Coat Technol 133–134:114
32. Holmberg K, Mattews A (1994) In: Dowson D (ed) Coatings tribology, tribology series 28, 1st edn. Elsevier, Oxford, p 53
33. Zhitomirsky VN, Kim SK, Burstein L, Boxman RL (2010) Appl Surf Sci (in press)
34. Hofmann S, Sanz JM (1982) J Trace Microprobe Tech 1:213
35. Zhitomirsky VN, Zarchin O, Wang SG, Boxman RL, Goldsmith S (2001) IEEE Trans Plasma Sci 29:776
36. Zhitomirsky VN, Boxman RL, Goldsmith S (1995) J Vac Sci Technol A13:2233
37. Zhitomirsky VN, Kinrot U, Alterkop B, Boxman RL, Goldsmith S (1996) Surf Coat Technol 86–87:263
38. Rosen J, Persson POA, Ionescu M, Pigott J, McKenzie DR, Bilek MMM (2007) Plasma Chem Plasma Proc 27:599
39. Bolt H, Koch F, Rodet JL, Karpov D, Menzel S (1999) Surf Coat Technol 116–119:956
40. Niu EW, Li L, Lv GH, Chen H, Li XZ, Feng WR, Fan SH, Yang SZ, Yang XZ (2007) Mater Sci Eng A460:135
41. Niu EW, Li L, Lv GH, Chen H, Li XZ, Fan SH, Yang SZ, Yang XZ (2008) Appl Surf Sci 254:3909
42. Mattox MD (2000) Surf Coat Technol 133–134:517
43. Shtansky DV, Kaneko K, Ikuhara Y, Levashov EA (2001) Surf Coat Technol 148:206